Petroleum Science 20 (2023) 2575–2584

Contents lists available at ScienceDirect

Petroleum Science

journal homepage: www.keaipublishing.com/en/journals/petroleum-science

Original Paper

Impacts of support properties on the vacuum residue slurry-phase hydrocracking performance of Mo catalysts

Wei-Wei Feng [a], Ye-Gui Qian [a], Ting-Hai Wang [a], Qing-Yan Cui [a, *], Yuan-Yuan Yue [a], Pei Yuan [a], Xiao-Jun Bao [b]

[a] College of Chemical Engineering, Fuzhou University, Fuzhou, Fujian, 350116, China
[b] Qingyuan Innovation Laboratory, Quanzhou, Fujian, 362801, China

ARTICLE INFO

Article history:
Received 4 October 2022
Received in revised form
9 December 2022
Accepted 23 February 2023
Available online 25 February 2023

Edited by Jia-Jia Fei

Keywords:
Slurry-phase hydrocracking
Vacuum residue
Supports
Catalytic performance

ABSTRACT

To deeply understand the effects of support properties on the performance of Mo-based slurry-phase hydrocracking catalysts, four Mo-based catalysts supported on amorphous silica alumina (ASA), γ-Al_2O_3, ultra-stable Y (USY) zeolite and SiO_2 were prepared by the incipient wetness impregnation method, respectively, and their catalytic performances were compared in the vacuum residue (VR) hydrocracking process. It is found that the Mo/ASA catalyst exhibits the highest VR conversion among the different catalysts, indicating that both the appropriate amount of acid sites, especially B acid sites and larger mesoporous volume of ASA can enhance the VR hydrocracking into light distillates. Furthermore, Mo catalysts supported on the different supports show quite different product distributions in VR hydrocracking. The Mo/ASA catalyst provides higher yields of naphtha and middle distillates and lower yields of gas and coke compared with other catalysts, it is attributed to the highest MoS_2 slab dispersion, the highest sulfuration degree of Mo species, and the most Mo atoms located at the edge sites for the Mo/ASA catalyst, as observed by HRTEM and XPS analyses. These features of Mo/ASA are beneficial for the hydrogenation of intermediate products and polycyclic aromatic hydrocarbons to restrict the gas and coke formation.

1. Introduction

Fast depletion of conventional crude oil reserves and increasing demand for clean transportation fuels greatly stimulate the research and development of heavy oil upgrading technologies (Bellussi et al., 2013; Browning et al., 2021; Saab et al., 2020). Efficient conversion of vacuum residue (VR), the heaviest fraction of crude oil, into lighter fractions such as gasoline and diesel is considered as one of the greatest challenges in the modern petroleum processing industry (Omajali et al., 2017; Prajapati et al., 2021). VR is mainly comprised of high boiling point polycyclic aromatic hydrocarbons with large amount of sulfur (S), nitrogen (N), and metals (usually vanadium (V) and nickel (Ni)) (Pham et al., 2022; Prajapati et al., 2022), resulting in coke formation on both catalyst and equipment in the refining process (Tsubaki et al., 2002; Fortain et al., 2010; Kim et al., 2017). Among the various VR conversion technologies developed up to date, slurry-phase hydrocracking technology is considered as the most efficient and economic one because of its great feedstock flexibility, high conversion efficiency, and high light distillates yield. It is recognized that catalyst is the key in this process, because it determines the feedstock conversion and the liquid product yield (Saab et al., 2020; Morawski and Mosiewski, 2006; Looi et al., 2012).

Slurry-phase hydrocracking catalysts include homogeneously dispersed catalysts of oil-soluble dispersed catalysts and water-soluble dispersed catalysts and heterogeneous solid powder catalysts (Purón et al., 2013; Nguyen et al., 2015). Oil-soluble dispersed catalysts exist as organometallic compounds can effectively depress the gas and coke formation due to its homogeneously dispersed heavy oil to adequately contact with reactant molecule (Chen et al., 2022; Kang et al., 2019). Water-soluble dispersed catalysts are prepared with multiple steps such as dispersion, emulsification and dehydration, which greatly increase the operation complexity and cost (Liu et al., 2009; Luo et al., 2011). Natural mineral catalysts as solid powder catalysts, which have the

* Corresponding author.
E-mail address: qycui@fzu.edu.cn (Q.-Y. Cui).

https://doi.org/10.1016/j.petsci.2023.02.029

advantages of low cost and broad sources, were extensively used in the early stage of slurry-phase hydrocracking technology. Nevertheless, they were replaced gradually by other types of catalysts due to their inferior catalytic activities and property instability (Yue et al., 2016, 2018; Manek and Haydary, 2017). Supported metal catalysts are composed of active metal and support, in which the active metals are usually Mo, Co, Ni or their binary/trinary combinations, and the supports are commonly acidic materials such as alumina, silica-alumina, zeolites and even natural minerals (Looi et al., 2012; Leyva et al., 2007, 2009). As compared with natural mineral catalyst, supported metal catalyst has the advantages on the enhancement of hydrocracking reactivity and adjustable performance, thus it has attracted increasing attention in slurry-phase hydrocracking.

In supported metal catalysts, the metal species are considered as the active centers to hydrogenate the polycyclic aromatic hydrocarbons and olefins, and to quench the free radicals in the feedstock and intermediate products to avoid the over-cracking reactions and condensation reactions to form gas and coke. In addition, the support also plays a crucial role in determining the catalytic performance by affecting the metal dispersion on the catalyst surface and thus influencing the feedstock conversion. There were many reports on supported catalysts employed in the slurry-phase hydrocracking process. The MoS_2/SiO_2–ZrO_2 bifunctional catalyst was applied in the slurry-phase hydrocracking of decalin-phenanthrene mixture to study the effect of Si/Zr molar ratio on performance of catalyst, the analysis results revealed that Brönsted acid on SiO_2–ZrO_2 support was mainly contributed to the catalytic performance (Ma et al., 2021). Looi et al. (2012) prepared a series of catalysts using alumina supports with different pore sizes and investigated their catalytic performance in residual oil hydrocracking, the result showed that the residue oil conversion was about 50 wt% and the highest yield of liquid products was 97 wt% at 400 °C, and more acid sites benefited to the residue oil conversion. Yue et al. (2018) prepared the slurry-phase hydrocracking catalyst by using a hydrothermally treated natural bauxite mineral as the support and assessed their performance by using a high temperature coal tar as the feedstock, and they found that the high feedstock conversion and high liquid yield were attributed to the suitable support acidity and the weaker interaction between the active metal and the support. Sánchez et al. (2018) investigated the catalytic performance of a bifunctional MoS_2/ASA (amorphous silica-alumina) catalyst in the slurry-phase hydroconversion, and found that the presence of moderate Brönsted acid sites promoted the cracking, isomerization and ring-opening reactions. Despite numerous reports available on supported slurry-phase hydrocracking catalysts, there is a lack of systematic and deep understanding on the influences of support properties such as composition, pore structure and acidity on catalytic performance.

Herein, we present a thorough study on the effects of support properties on the catalytic performance of supported metal catalysts in the VR slurry-phase hydrocracking process. A series of Mo catalysts supported on SiO_2, γ-Al_2O_3, amorphous silica-alumina (ASA) and ultra-stable Y (USY) zeolite, respectively, were prepared by the conventional impregnation method. The pore structure and acidity of the different supports were examined by N_2-adsorption-desorption and pyridine adsorbed Fourier transform infrared (Py-FTIR) spectroscopy, the morphology of metal sulfide species on the corresponding catalysts were investigated by high resolution transmission electron microscopy (HRTEM), and the catalytic performances of the different catalysts were compared in the VR slurry-phase hydrocracking.

2. Experimental

2.1. Catalyst preparation

In the present study, SiO_2, γ-Al_2O_3, ASA and USY zeolite with Si/Al ratio of 2.7 were used as the supports to prepare slurry-phase hydrocracking catalysts. SiO_2, γ-Al_2O_3 and USY zeolite were obtained from Shanghai Aladdin Bio-Chem Technology Co. Ltd., Fujian Yucheng Environmental Protection Technology Co. Ltd. and Nankai University, respectively. ASA was prepared as follows: 25 mL of an aluminum nitrate solution with a concentration of 2 mol/L and 30 mL ammonia water (25 wt% of ammonia) were simultaneously and slowly added into 50 mL water to maintain pH value of 8–9 at 60 °C under agitation. Then, 2.7 g of sodium silicate (27.68% SiO_2 and 8.95% Na_2O) was added into the above solution to obtain a mixture with a SiO_2/Al_2O_3 molar ratio of 1:1. Finally, the resulting mixture was aged for 1 h, filtered with distilled water, dried at 120 °C for 10 h, and calcined at 500 °C for 3 h to obtain ASA sample.

A series of catalysts supported on the different materials were prepared by the conventional incipient wetness impregnation method with an aqueous solution of ammonium molybdate tetrahydrate ($(NH_4)_6Mo_7O_{24}\cdot 4H_2O$, 98%, Adamas). The resultant samples were aged at 30 °C for 12 h, dried at 120 °C for 10 h, and calcined at 600 °C for 4 h to obtain the corresponding supported Mo oxide catalysts, which are designated as Mo/SiO_2, Mo/USY, Mo/γ-Al_2O_3 and Mo/ASA, respectively. The MoO_3 content in each catalyst is 5 wt% according to the literature (Kim et al., 2018; Ancheyta et al., 2003).

2.2. Characterizations

N_2 adsorption-desorption measurement was taken on a Micromeritics ASAP 2460 apparatus at −196 °C. The surface area (S_{BET}) of sample was determined by using Brunauer-Emmett-Teller (BET) equation, and the pore volumes (V_{total}) and average pore diameters (D_p) were obtained by Barrett-Joyner-Halenda (BJH) method. Adsorbed pyridine Fourier transform infrared spectroscopy (Py-FTIR) measurement was carried out on a MAGNAIR 560 FTIR instrument, and the spectra were recorded at 250 and 350 °C, respectively. H_2 temperature programmed reduction (H_2-TPR) was conducted on an ASAP-2920 equipment using a thermal conductivity detector (TCD). Around 20 mg of sample was firstly pretreated in Ar steam at 300 °C for 30 min, and then cooled to 50 °C. The H_2-TPR profiles were acquired from 50 to 950 °C at a heating rate of 10 °C/min in a 10 vol% H_2/Ar stream.

High resolution transmission electron microscopy (HRTEM) images of MoS_2 slabs were collected on a Tecnai G2 F20 instrument at 200 kV, and at least 200 slabs were measured to for each sample. The average lengths ($\overline{L}$) and stacking numbers ($\overline{M}$) according to the Eqs. (1) and (2) (Liu et al., 2017; Escobar et al., 2018):

$$\text{Average slab length}: \overline{L} = \frac{\sum_{i=1}^{n} x_i L_i}{\sum_{i=1}^{n} x_i} \tag{1}$$

$$\text{Average stack number}: \overline{M} = \frac{\sum_{i=1}^{n} x_i m_i}{\sum_{i=1}^{n} x_i} \tag{2}$$

where L_i, x_i and m_i denote the length, the number and the layer number in a stack of MoS_2 slabs.

The MoS_2 dispersion (D_{Mo}) was acquired by Eq. (5), f_{Moe} is the ratio of Mo atoms located at edge sites of MoS_2 slabs, and f_{Moc} is the fraction of Mo atoms at corner sites, which were estimated by Eqs. (3) and (4) (Hensen et al., 2001; Kasztelan et al., 1984):

$$f_{Moe} = \frac{Mo_{edge}}{Mo_{total}} = \frac{\sum_{i=1}^{t} 6(x_i - 2)}{\sum_{i=1}^{t} (3x_i^2 - 3x_i + 1)} \tag{3}$$

$$f_{Moc} = \frac{Mo_{corner}}{Mo_{total}} = \frac{6}{\sum_{i=1}^{t} (3x_i^2 - 3x_i + 1)} \tag{4}$$

$$D_{Mo} = f_{Moe} + f_{Moc} = \frac{Mo_{edge} + Mo_{corner}}{Mo_{total}} = \frac{\sum_{i=1}^{t} 6(x_i - 1)}{\sum_{i=1}^{t} (3x_i^2 - 3x_i + 1)} \tag{5}$$

where Mo_{edge}, Mo_{corner} and Mo_{total} are the numbers of Mo atoms along on edge sites, corner sites and total Mo atoms on MoS_2 slabs, t represents the total number of slabs, and x_i denotes the number of Mo atoms on edge sites of each MoS_2 slab, acquired by $L_i = 3.2 \times (2x_i - 1)$.

X-ray photoelectron spectroscopy (XPS) was taken on a Thermo ESCALAB 250 spectrometer with a monochromatic Al Kα source. C 1s peak at 284.6 eV was used as reference to calibrate the binding energy. The XPSPEAK41 software was employed to analyze the experimental results. The relative contents of each species of MoS_2, MoS_xO_y and Mo^{6+} oxide for an individual sulfide catalyst were determined through their peak areas. For instance, the relative MoS_2 content [MoS_2] (%) was calculated by Eq. (6):

$$[MoS_2](\%) = \frac{A_{MoS_2}}{A_{MoS_2} + A_{MoSxOy} + A_{Mo^{6+}}} \times 100\% \tag{6}$$

where A_X represents the peak area of species X in Mo 3d XPS envelope.

2.3. Catalytic assessment

VR provided by SINOCHEM Quanzhou PetroChemical Co., Ltd. was employed as the feedstock to assess the slurry-phase hydrocracking performance of catalysts, and its properties are shown in Table 1.

Table 1
Properties of VR used in the hydrocracking.

Properties	Values
Density, kg m^{-3} (20 °C)	985.5
Viscosity, cSt (100 °C)	84.7
Ni, ppm	46.2
V, ppm	111
S, wt%	3.1
N, ppm	3427
Conradson carbon residue, wt%	10.7
Boiling point range, °C	
< 180	0.0
180–350	2.1
350–520	31.4
> 520	66.5

The catalyst assessment for VR hydrocracking was carried out in a 300 mL stainless-steel autoclave equipped with a stirrer. 40 g of VR, 1.2 g of catalyst and 0.88 g of sulfur powder were added into the reactor. Prior to the hydrocracking reaction, the sulfuration of catalyst *in situ* was conducted at 350 °C under an initial H_2 pressure of 11 MPa for 5 h, subsequently, the VR hydrocracking reaction was performed at 430 °C with a volumetric H_2 to oil ratio of 850 (*v*/*v*) for 3 h under a stirring rate of 600 rpm. After reaction, the mixture of the reaction product and catalyst was collected after the autoclave rapidly cooled to room temperature and was separated by centrifugalization and filtration. The liquid product was divided into four fractions in a SYD-9168 vacuum distillation apparatus according to the boiling point (BP) range, the four fractions of naphtha, middle distillate, vacuum gas oil (VGO) and VR are in the range of BP < 180 °C, 180–350 °C, 350–500 °C and BP > 500 °C. Additionally, the solid residue including coke and the used catalyst was washed with toluene. The VR conversion and the yields of gas, naphtha, middle distillate, VGO and coke were acquired by the following Eqs. (7)–(12):

$$\text{VR conversion(wt\%)} = \frac{M_f - M_p}{M_f} \times 100\% \tag{7}$$

$$\text{Gas yield(wt\%)} = \frac{M_g}{M_t} \times 100\% \tag{8}$$

$$\text{Naphtha yield(wt\%)} = \frac{M_n}{M_t} \times 100\% \tag{9}$$

$$\text{Middle distillate yield(wt\%)} = \frac{M_m}{M_t} \times 100\% \tag{10}$$

$$\text{VGO yield(wt\%)} = \frac{M_v}{M_t} \times 100\% \tag{11}$$

$$\text{Coke yield(wt\%)} = \frac{M_c}{M_t} \times 100\% \tag{12}$$

where M_f, M_p are mass of > 500 °C fraction in the feed and product, M_g, M_n, M_m, M_v and M_c denote mass of gas, < 180 °C fraction, 180–350 °C fraction, 350–500 °C fraction, and coke in product, meanwhile, M_t means the total mass of feed.

3. Results and discussion

3.1. Catalytic performance

VR slurry-phase hydrocracking performance of Mo catalysts supported on the different supports was assessed, and the resulting product was distilled to obtain the different distillate fractions. The VR conversions and the yields of naphtha and middle distillate obtained over different catalysts are shown in Fig. 1. It can be seen that the VR conversion over Mo/ASA is 75.2%, only slightly higher than those (73.9% and 73.5%) over Mo/γ-Al_2O_3 and Mo/USY, but significantly higher than that (67.4%) over Mo/SiO_2. The results demonstrate that, as compared with the other catalysts, Mo/ASA can effectively convert the heavy fraction with large molecules in VR into lighter fractions with smaller molecules. The yields of naphtha and middle distillate over the different catalysts are in the order of Mo/ASA > Mo/γ-Al_2O_3 ≈ Mo/USY > Mo/SiO_2, indicating that Mo/ASA favors the production of naphtha and middle distillate.

Fig. 2 displays the yields of naphtha, middle distillate, VGO, gas

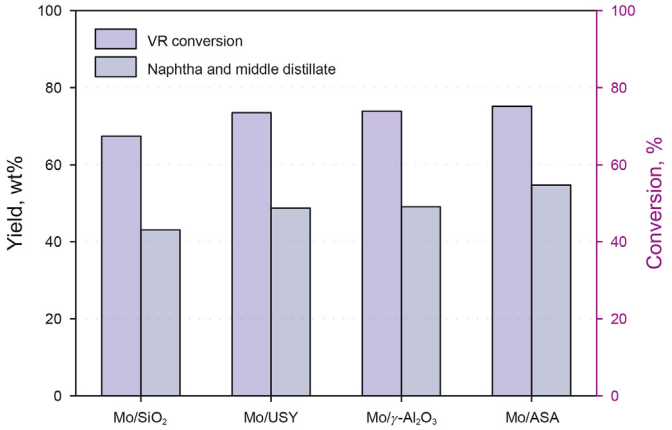

Fig. 1. VR conversions and the yields of naphtha and middle distillate obtained over the different catalysts.

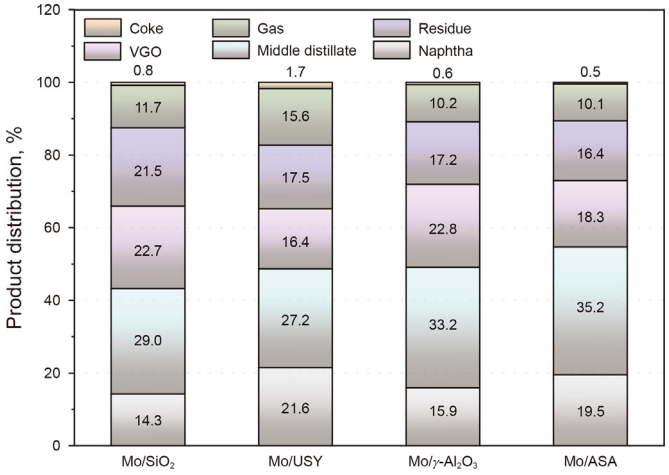

Fig. 2. Product distributions obtained over the different catalysts.

and coke obtained over the different catalysts. The naphtha yield over Mo/ASA is 19.5 wt%, slightly lower than that (21.6 wt%) over Mo/USY, but obviously higher than those (14.3 wt% and 15.9 wt%) over Mo/SiO_2 and $Mo/\gamma\text{-}Al_2O_3$, while the middle distillate yield over Mo/ASA is 35.2 wt%, much higher than those over the others. The VGO yields obtained over the different catalysts follow the order of $Mo/\gamma\text{-}Al_2O_3$ (22.8 wt%) ≈ Mo/SiO_2 (22.7 wt%) > Mo/ASA (18.3 wt%) > Mo/USY (16.4 wt%). The yields of unconverted residue decrease in the order of Mo/SiO_2 (21.5 wt%) > Mo/USY (17.5 wt%) ≈ $Mo/\gamma\text{-}Al_2O_3$ (17.2 wt%) > Mo/ASA (16.4 wt%). The yields of gas are in the order of Mo/USY (15.6 wt%) > Mo/SiO_2 (11.7 wt%) > $Mo/\gamma\text{-}Al_2O_3$ (10.2 wt%) ≈ Mo/ASA (10.1 wt%), and the yields of coke increase in the order of Mo/ASA (0.5 wt%) ≈ $Mo/\gamma\text{-}Al_2O_3$ (0.6 wt%) < Mo/SiO_2 (0.8 wt%) < Mo/USY (1.7 wt%). By comparing the above results, it is concluded that Mo/ASA exhibits the best overall performance among all the catalysts due to its highest VR conversion, highest yield of naphtha and middle distillate, and relatively lower yields of gas and coke.

The hydrogen consumption can be considered as an index of catalyst hydrogenation activity, because VR slurry-phase hydrocracking reaction is accompanied with hydrogen consumption (Bianco et al., 1994; Kang et al., 2020). Fig. 3 shows the H_2 pressure profiles during the VR slurry-phase hydrocracking process involving the different catalysts. Before the reaction, the initial H_2 pressure in the reactor was 11.0 MPa at room temperature, when the reaction temperature was increased to 430 °C, the pressure in reactor increased up to 21.5 MPa, then the pressure in reactor gradually decreased with the prolonging reaction time, and the decreasing tendencies were different for the reaction systems involving the different catalysts. After the hydrocracking reaction was terminated by cooling the reactor to about 200 °C, the pressures in the reactors loaded with different catalysts were dramatically dropped, the residual pressures were in the order of Mo/ASA < Mo/USY < $Mo/\gamma\text{-}Al_2O_3$ < Mo/SiO_2. This indicated that Mo/ASA has the highest hydrogenation activity among the four catalysts. The Mo catalysts on the different support present different slurry-phase hydrocracking performances, thus it is necessary to deeply analyze properties and pore structures of these supports and their derived catalysts to understand the underlying reasons.

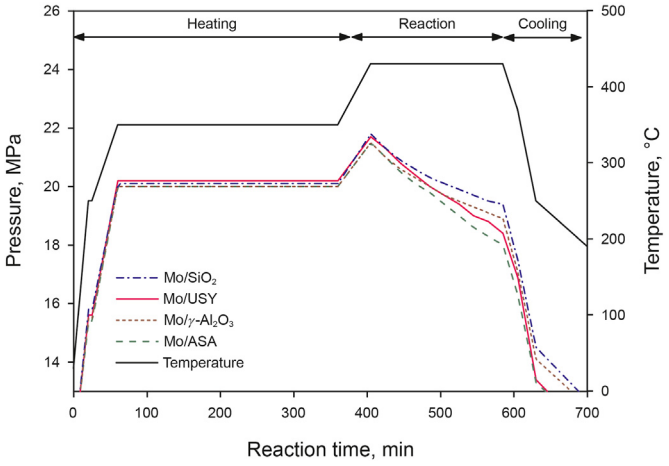

Fig. 3. H_2 pressure change profiles in the reactors loaded with different catalysts.

3.2. Characterizations of supports

3.2.1. Textural properties

The textural properties of catalysts can significantly impact their VR hydrocracking performance. It is widely accepted that macro-/meso-porous structure in supported catalysts benefits the diffusion of bulkier molecules in VR and thereby provides higher accessibility of active sites to reactants molecules, promoting feedstock conversion and improving the selectivity to target products (Leyva et al., 2014; Zheng et al., 2019). To understand the effects of pore structures of the supports on the catalytic performance of their derived catalysts, N_2 adsorption-desorption measurements were conducted to compare the textural properties of the different supports, and the results are shown in Fig. 4. It can be seen that the N_2 adsorption-desorption isotherms of USY zeolite and $\gamma\text{-}Al_2O_3$ belong to type II ones with a H4 hysteresis loop, but those of SiO_2 and ASA belong to type IV ones with a H1 hysteresis loop and a H3 hysteresis loop, respectively, indicating that the different supports have different pore structures. The surface areas, pore volumes and average pore diameters of the different supports calculated from the N_2 adsorption-desorption data are summarized in Table 2. It is seen that the surface area (585 m^2/g) of USY zeolite is much larger than those (386 m^2/g, 198 m^2/g, and 226 m^2/g) of ASA, $\gamma\text{-}Al_2O_3$ and SiO_2, whereas ASA has the largest external surface area (357 m^2/g) among all the supports, with USY zeolite having the smallest external surface area (52 m^2/g). The average pore volumes of different supports are in the order of SiO_2 (0.89 cm^3/g) > ASA (0.76 cm^3/g) > USY zeolite (0.34 cm^3/g) > $\gamma\text{-}Al_2O_3$ (0.25 cm^3/g), but

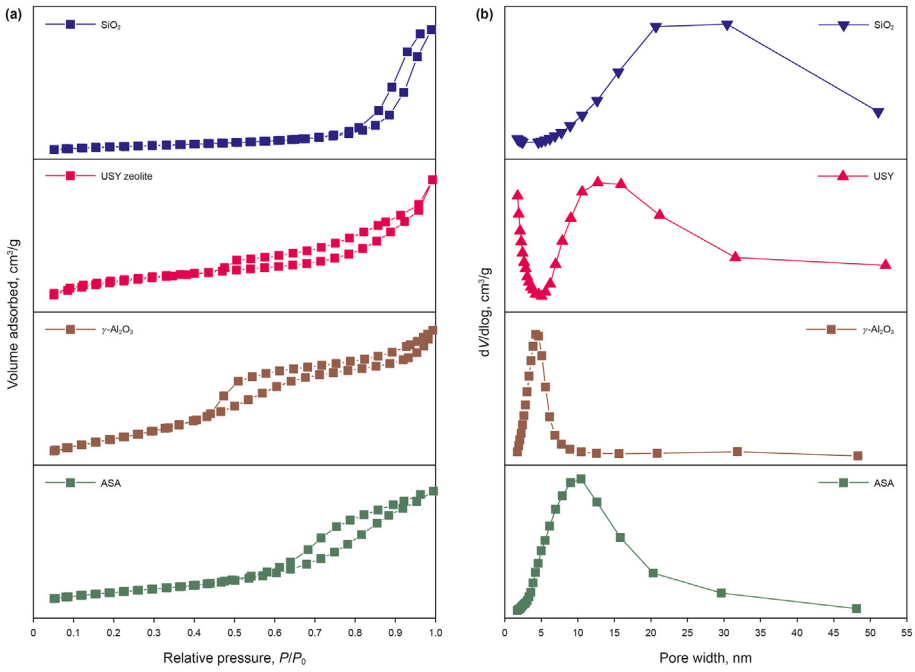

Fig. 4. N_2 adsorption-desorption isotherms (**a**) and pore size distribution (**b**) of the different supports.

Table 2
Textural parameters of the different supports.

Samples	S_{BET}, $m^2\ g^{-1}$		V_p, $cm^3\ g^{-1}$		D_p, nm	Si/Al ratio
	S_{total}	S_{ext}	V_{total}	V_{meso}		
SiO_2	226	206	0.89	0.88	17.9	–
USY zeolite	585	52	0.34	0.07	2.3	2.7
γ-Al_2O_3	198	154	0.25	0.17	4.6	–
ASA	386	357	0.76	0.75	7.7	0.5

their mesoporous volumes are in the order of SiO_2 (0.88 cm^3/g) > ASA (0.75 cm^3/g) > γ-Al_2O_3 (0.17 cm^3/g) > USY zeolite (0.07 cm^3/g). These results suggest that, among different supports, ASA that simultaneously has the largest external surface area, larger average pore volume and mesoporous volume should be the most suitable for the preparing slurry-phase hydrocracking catalyst, because its larger average pore volume and mesoporous volume are beneficial for the diffusion of bulkier molecules in VR and their generated intermediate molecules onto the active sites of catalyst, and its largest external surface area favors metal dispersion and thereby generates more active metal sites to restrain gas and coke formation, this can provide the highest VR conversion, highest total yield of naphtha and middle distillate, and lowest yields of coke and gas obtained over Mo/ASA, as shown in Figs. 1 and 2.

3.2.2. Acidity

The acid properties of the different supports were characterized by Py-FTIR, the results measured at 250 and 350 °C are shown in Fig. 5. The bands at 1540 and 1450 cm^{-1} are attributed to Brönsted and Lewis acid sites, respectively (Schweitzer et al., 2022). The Py-FTIR spectrum of USY zeolite has a stronger adsorption peak at 1540 cm^{-1} and a weaker adsorption peak at 1450 cm^{-1}, indicating that USY zeolite has a large amount of B acid sites, ascribed to the bridging Si–OH–Al groups because of the replacement of Si^{4+} in the crystallite framework by Al^{3+} (Tang et al., 2019). However, it has only a very small amount of L acid sites. The spectrum of γ-Al_2O_3 has an adsorption peak at 1450 cm^{-1} but no apparent peak at 1540 cm^{-1}, and that of ASA has two weaker peaks at 1450 and 1540 cm^{-1} for both 250 and 350 °C, illustrating the existence of small amounts of B and L acid sites in ASA. No obvious pyridine adsorption peak is observed for SiO_2, indicating its negligible acid sites. The amounts of acid sites calculated according to Py-FTIR spectra measured at 250 and 350 °C for the different supports are summarized in Table 3. Notably, the acid sites determined at 250 °C are considered as weak ones, while the acid sites determined at 350 °C can be taken as moderate and strong ones (Gafurov et al., 2015; Phung and Busca, 2015). No acid site exists in SiO_2, as shown in Table 3, and the USY zeolite has the largest amount of acid sites including weak, moderate and strong ones, especially B acid sites. Thus, γ-Al_2O_3 and ASA present the total acid amounts standing between those of SiO_2 and the USY zeolite, with the former having only L acid sites and the latter having only a smaller amount of L acid sites but a larger amount of B acid sites, which is ascribed to the bridging hydroxyls in connection with tetrahedrally coordinated Al species on silica (Valla et al., 2015). It indicates the amounts of acid sites in the different supports are in the order of USY zeolite > γ-Al_2O_3 > ASA > SiO_2.

By comparing the acidity characterization results and the hydrocracking reaction results in Figs. 1 and 2, it is found that Mo/SiO_2 prepared from SiO_2 with the largest average pore volume and mesoporous volume but without acid sites gives the lowest VR conversion among the different catalysts. Mo/USY prepared from USY zeolite with the smallest external surface area and mesoporous volume but with the largest amount of acid sites displays a higher VR conversion than Mo/SiO_2. Mo/γ-Al_2O_3 prepared from γ-Al_2O_3 with a relatively larger external surface area and a slightly larger mesoporous volume but with a larger amount of L acid sites, gives a VR conversion comparable to that of Mo/USY but much lower yields of gas and coke than Mo/USY. Mo/ASA prepared from ASA with the largest external surface area, larger mesoporous volume and more B and L acid sites presents the highest VR conversion, the highest yields of naphtha and middle distillate, and the yields of gas and coke comparable to that of Mo/Al_2O_3 but much lower than those of

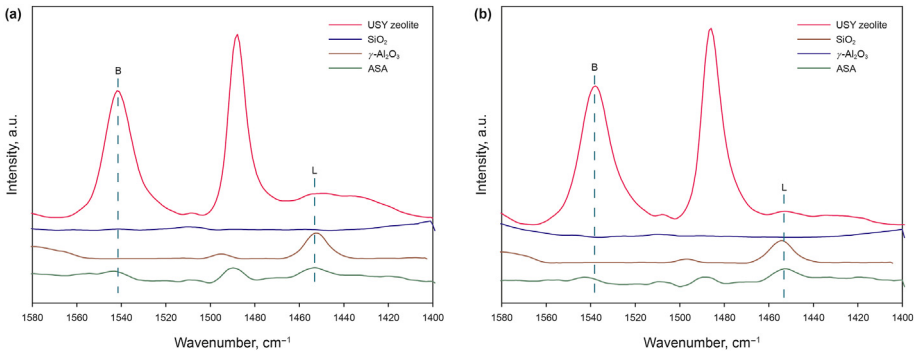

Fig. 5. Py-FTIR spectra of the different supports measured at (**a**) 250 °C and (**b**) 350 °C.

Table 3
Acid properties of the four supports.

Samples	Temperature, °C	L, μmol/g	B, μmol/g	L + B, μmol/g
SiO_2	250	0.0	0.0	0.0
	350	0.0	0.0	0.0
USY zeolite	250	14.0	606.8	620.8
	350	7.4	549.7	557.1
γ-Al_2O_3	250	74.3	0.0	74.3
	350	52.1	0.0	52.1
ASA	250	24.4	15.9	40.3
	350	22.8	11.3	34.1

Mo/SiO_2 and Mo/USY. Therefore, it can be concluded that both support acidity and pore structure can significantly impact VR conversion and the distribution of various distillates of hydrocracking product. By further comparing the acidity properties of ASA and γ-Al_2O_3, and the catalytic performance of their corresponding supported catalysts, it is interesting to note that, despite of the lower amount of acid sites of ASA than γ-Al_2O_3, Mo/ASA shows a slightly higher VR conversion, because ASA has abundant B acid sites and a larger mesoporous volume that can promote the hydrocracking reactions of VR following the carbenium ion mechanism (Weitkamp, 2012).

3.3. Characterization of catalysts

3.3.1. H_2-TPR

The reducibility of Mo species on the four supported catalysts were investigated by H_2-TPR and the results are given in Fig. 6. In the H_2-TPR profiles, two H_2 reduction peaks are observed: the low-temperature peak can be attributed to the reduction of octahedrally coordinated Mo^{6+} species to tetrahedrally coordinated Mo^{4+} species, and the high-temperature peak can be assigned to the further reduction of tetrahedrally coordinated Mo^{4+} species to Mo (Wang et al., 2002; Liu et al., 2012; Lv et al., 2018; Zhang et al., 2019). The low-temperature peaks of the four catalysts are in the range of 400–500 °C and shift to high temperatures in the order of Mo/ASA < Mo/γ-Al_2O_3 < Mo/USY < Mo/SiO_2. It is also noted that the high temperature reduction peaks of Mo/ASA, Mo/SiO_2 and Mo/γ-Al_2O_3 are centered at 816, 820 and 857 °C, respectively, whereas no obvious high temperature reduction is observed for Mo/USY. This suggests that the reducibilities of Mo species in the four catalysts are different, possibly due to the different metal-support interaction (Fan et al., 2007). Generally, it is considered that the ability of a metal oxide to adsorb and activate hydrogen is related to the reduction temperature, and a metal oxide that can be easily reduced by hydrogen usually has a higher hydrogenation activity

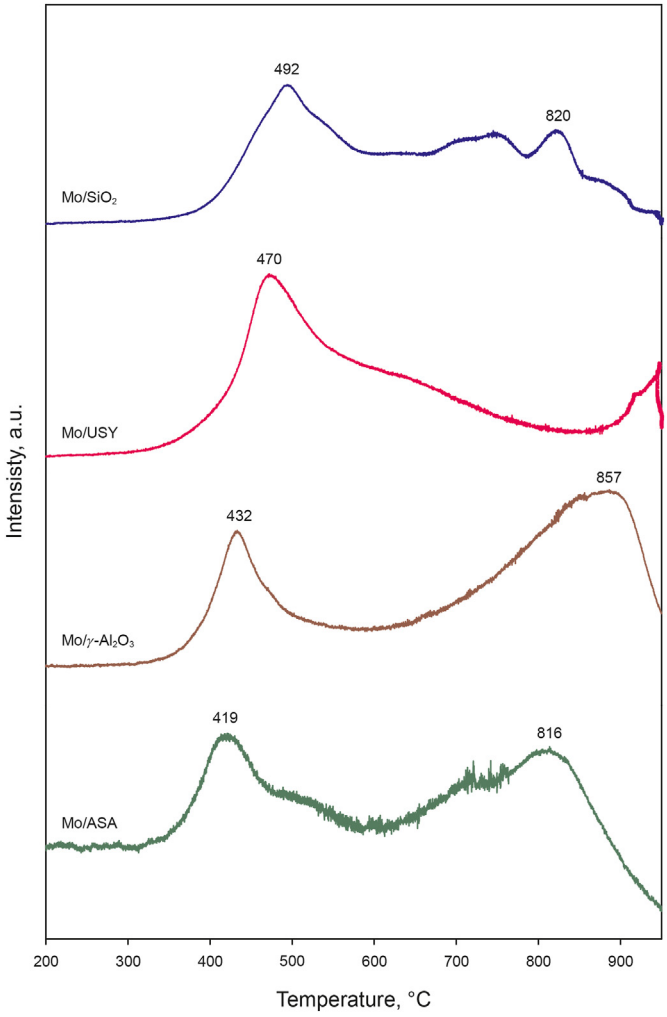

Fig. 6. H_2-TPR profiles of the catalysts supported on the different supports.

(Cheng et al., 2020). Therefore, the higher yields of naphtha and middle distillate and the lower yields of gas and coke obtained over Mo/ASA can be attributed to the easier reduction of Mo species in Mo/ASA.

3.3.2. HRTEM

HRTEM characterization was performed to observe the morphology of MoS_2 slabs as the active phase in the hydrocracking reaction, the representative images obtained are shown in Fig. 7.

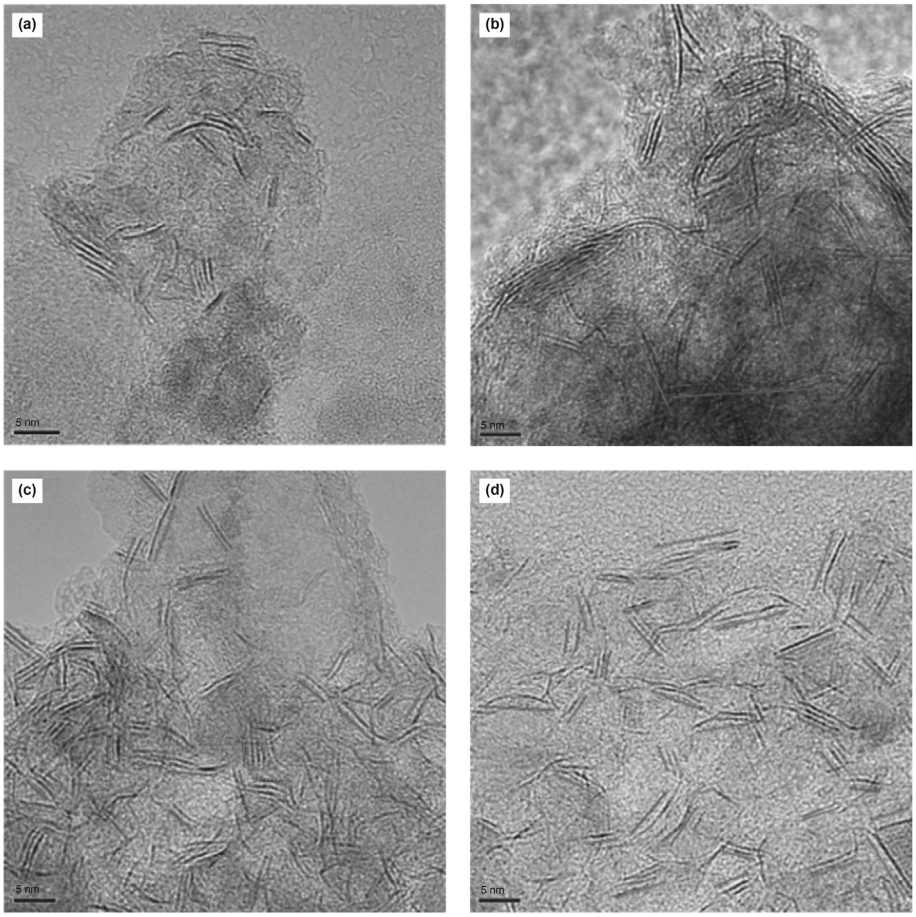

Fig. 7. HRTEM images of the sulfide catalysts: (**a**) Mo/SiO_2, (**b**) Mo/USY, (**c**) Mo/γ-Al_2O_3 and (**d**) Mo/ASA.

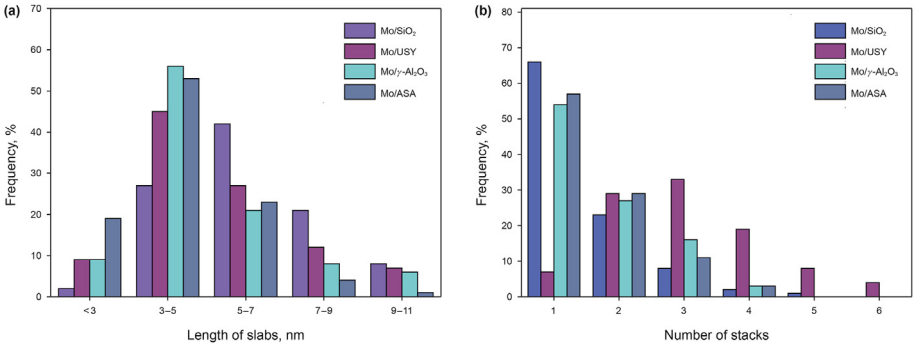

Fig. 8. Length distributions (**a**) and stacking number distributions (**b**) of MoS_2 slabs.

Table 4
Statistics results of MoS_2 slabs on the different sulfide catalysts.

Catalysts	$\bar{L}$, nm	$\bar{N}$	f_{Moe}	f_{Moc}	D_{Mo}
Mo/SiO_2	6.2	1.5	0.17	0.02	0.19
Mo/USY	5.2	3.0	0.20	0.03	0.23
Mo/γ-Al_2O_3	4.8	1.7	0.21	0.04	0.25
Mo/ASA	4.3	1.6	0.23	0.04	0.27

The statistical results of the lengths and stacking numbers of MoS_2 slabs are presented in Fig. 8 and Table 4. The two-dimensional thread-like fringes with layer stacking spacing of about 0.65 nm can be assigned as MoS_2 slabs (Zheng et al., 2019). The lengths of MoS_2 slabs are mainly from 3 to 7 nm for all catalyst, as shown in Fig. 8a. In addition, the average length of MoS_2 slabs on different catalysts reduces following of Mo/SiO_2 (6.2 nm) > Mo/USY zeolite (5.2 nm) > Mo/γ-Al_2O_3 (4.8 nm) > Mo/ASA (4.3 nm). It is found that the MoS_2 slabs on Mo/SiO_2, Mo/γ-Al_2O_3 and Mo/ASA are mainly stacked in 1–2 layers, but those on Mo/USY are mainly stacked in 2–5 layers, as shown in Fig. 8b. The average stacking number of MoS_2 slabs on Mo/USY catalyst is 3.0, obviously higher than those on the others (1.7 for Mo/SiO_2, 1.5 for Mo/γ-Al_2O_3 and 1.6 for Mo/ASA). The results reveal that Mo/ASA exhibits small MoS_2 particles with the lowest stacking number and the shortest slab length

among all catalysts, implying the more exposure active sites and the weaker space resistance that benefit to improve the hydrocracking activity (Liu et al., 2019). The dispersion degrees of Mo species (D_{Mo}) and the proportion of Mo species located along edge sites of MoS_2 slabs (f_{Moe}) with high hydrogenation activity were also estimated based on the HRTEM results. The values of D_{Mo} and f_{Moe} for the different catalysts increase as Mo/SiO_2 (0.17 and 0.19) < Mo/USY (0.20 and 0.23) < Mo/γ-Al_2O_3 (0.21 and 0.25) < Mo/ASA (0.23 and 0.27). The result indicates that the highest dispersion and the largest proportion of Mo species located along edge sites of MoS_2 slabs on Mo/ASA, possibly due to the appropriate interaction of ASA with Mo species. Generally, the D_{Mo} and f_{Moe} values of MoS_2 slabs can determine the hydrogenation activity of catalyst, because MoS_2 slabs with larger D_{Mo} and f_{Moe} values can expose more hydrogenation active sites, favoring the hydrogenation reaction to avoid over-cracking reaction and the condensation reaction of polycyclic aromatic hydrocarbons to yield gas and coke (Jiang et al., 2017). Therefore, the different yields of naphtha and middle distillate, gas and coke over the four catalysts can be attributed to their different D_{Mo} and f_{Moe} values.

3.3.3. XPS spectroscopy

The obtained Mo 3d XPS spectra and their deconvolution results are shown in Fig. 9 and Table 5. The Mo 3d XPS envelope includes three Mo 3d doublets, the doublet with binding energies at 229.0 ± 0.2 and 232.1 ± 0.2 eV for Mo $3d_{5/2}$ and Mo $3d_{3/2}$ are assigned to MoS_2 species (Mo^{4+}), the binding energies at 230.9 ± 0.2 and 234 ± 0.2 eV for Mo $3d_{5/2}$ and Mo $3d_{3/2}$ are related to MoS_xO_y oxysulfide compounds (Mo^{5+}), and the binding energies at 232.6 ± 0.2 and 235.8 ± 0.2 eV for Mo $3d_{5/2}$ and Mo $3d_{3/2}$ are attributed to MoO_3 species (Mo^{6+}) (Ninh et al., 2011). Table 5 lists the relative content of MoS_2 species that represents the sulfuration degree of Mo/SiO_2 (63%) < Mo/USY (66%) < Mo/γ-Al_2O_3 (70%) < Mo/ASA (74%). In view of the fact that the active Mo sites are generally located at edge and corner sites, and the hydrogenation reaction mainly occurs along the edge sites of MoS_2 crystals (Alsalme et al., 2016; Zheng et al., 2021), the contents of Mo atoms located at edge sites (Mo_e) in the different catalysts were calculated by $Mo_e = MoS_2 \times f_{Moe}$, the results are summarized in Table 5. It can be seen that the contents of Mo atoms located at edge sites are in the order of Mo/SiO_2 (10.7) < Mo/USY (13.2) < Mo/γ-Al_2O_3 (14.7) < Mo/ASA (17.0), indicating the hydrogenation activity increases following as the above tendency, it is consistent with HRTEM result. The XPS result demonstrates that the hydrocracking product distributions over the different catalysts are related with the sulfuration degrees and the contents of Mo atoms located at edges sites of Mo species. Mo/ASA catalyst with the highest sulfuration degree and content of Mo atoms located at edge sites of Mo species presents the highest hydrogenation activity to restrain the over-cracking reaction producing gas and the condensation reaction forming coke.

Table 5
Mo 3d XPS deconvolution results of the different sulfide catalysts.

Catalysts	Mo percentage, %			Mo_{sul}, %	Mo_e
	MoS_2	MoO_xS_y	MoO_3		
Mo/SiO_2	63	11	26	63	10.7
Mo/USY	66	8	26	66	13.2
Mo/γ-Al_2O_3	70	8	22	70	14.7
Mo/ASA	74	2	24	74	17.0

4. Conclusions

In this study, four Mo catalysts supported on four supports (ASA, γ-Al_2O_3, USY zeolite and SiO_2) were compared by investigating the effects of their pore structure, acidity and Mo species properties on their surface on the VR slurry-phase hydrocracking performance. The hydrocracking reaction results show that the VR conversions obtained over the four catalysts are in the order of Mo/ASA > Mo/γ-

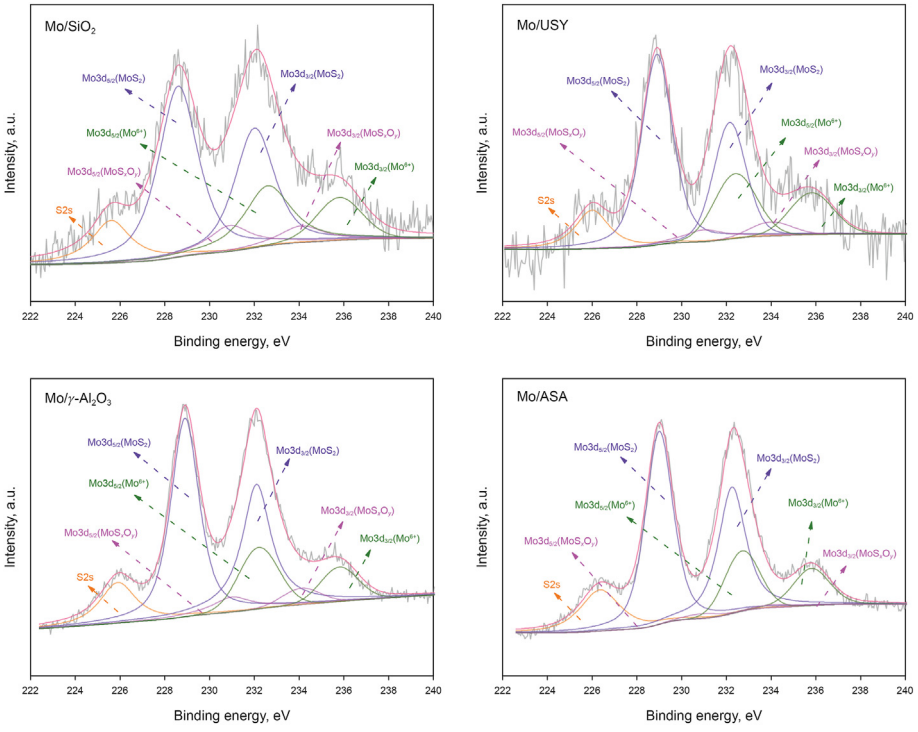

Fig. 9. Mo 3d XPS spectra and deconvolution results of the sulfide catalysts: in purple, MoS_2 contributions; in orange, MoS_xO_y contributions; in green, MoO_3 contributions.

$Al_2O_3 \approx$ Mo/USY > Mo/SiO_2, which is closely related to the acid site amounts and pore structures of supports. Moreover, the highest VR conversion over Mo/ASA is attributed to the larger mesoporous volume of ASA that is beneficial for the diffusion of the large molecules in VR to contact with the active sites on catalyst. Additionally, the appropriate amount of acid sites, especially B acid sites, of ASA enhances the catalytic cracking of VR. Therefore, both the appropriate amount of acid sites and larger mesoporous volume of supports are essential to catalytic activity. Importantly, the catalyst Mo/ASA exhibits the highest yield (54.7 wt%) of naphtha and middle distillate and the lowest yields (10.1 wt% and 0.5 wt%) of gas and coke among all catalysts, because the Mo species in Mo/ASA possess simultaneously the highest sulfuration degree, highest dispersion degree of MoS_2 slabs, and largest proportion of Mo atoms located at the edges sites. These features endow Mo/ASA with the highest hydrogenation activity, and thereby it can effectively restrain the over-cracking reaction of intermediate products and the condensation of polycyclic aromatic hydrocarbon to reduce the yields of gas and coke.

Declaration of competing interest

The authors declare that they have no known competing financial interests or personal relationships that could have appeared to influence the work reported in this paper.

Acknowledgments

The authors acknowledge National Key Research and Development Program of China (2018YFA0209403), National Natural Science Foundation of China (21908027) and Qingyuan Innovation Laboratory Program(00121002) for financing this research.

References

Alsalme, A., Alzaqri, N., Alsaleh, A., et al., 2016. Efficient Ni–Mo hydrodesulfurization catalyst prepared through Keggin polyoxometalate. Appl. Catal. B Environ. 182, 102–108. https://doi.org/10.1016/j.apcatb.2015.09.018.

Ancheyta, J., Betancourt, G., Centeno, G., et al., 2003. Catalyst deactivation during hydroprocessing of Maya heavy crude oil. (II) Effect of temperature during time-on-stream. Energy Fuel. 17 (2), 462–467. https://doi.org/10.1021/ef0201883.

Bellussi, G., Rispoli, G., Landoni, A., et al., 2013. Hydroconversion of heavy residues in slurry reactors: developments and perspectives. J. Catal. 308, 189–200. https://doi.org/10.1016/j.jcat.2013.07.002.

Bianco, A.D., Panariti, N., Carlo, S.D., et al., 1994. New developments in deep hydroconversion of heavy oil residues with dispersed catalysts. 2. kinetic aspects of reaction. Energy Fuel. 8 (3), 593–597. https://doi.org/10.1021/ef00045a013.

Browning, B., Alvarez, P., Jansen, T., et al., 2021. A review of thermal cracking, hydrocracking, and slurry phase hydroconversion kinetic parameters in lumped models for upgrading heavy oils. Energy Fuel. 35 (19), 15360–15380. https://doi.org/10.1021/acs.energyfuels.1c02214.

Chen, Y.F., Lu, Y.K., Guan, Z.K., et al., 2022. Ultrafine Co-MoS_2 monolayer catalyst derived from oil-soluble single-molecule polyoxometalates for slurry phase hydrocracking. Fuel 315, 123134–123148. https://doi.org/10.1016/j.fuel.2022.123134.

Cheng, Z.F., Wang, F.J., Yang, W.X., et al., 2020. Study of bimetallic NiFe catalysts for methyl laurate hydrogenation. J. Fuel Chem. Technol. 48 (7), 860–866. https://doi.org/10.1016/S1872-5813(20)30059-1.

Escobar, J., Barrera, M.C., Gutiérrez, A.W., et al., 2018. Highly active P-doped sulfided NiMo/alumina HDS catalysts from Mo-blue by using saccharose as reducing agents precursor. Appl. Catal. B Environ. 237, 708–720. https://doi.org/10.1016/j.apcatb.2018.06.034.

Fan, Y., Bao, X.J., Wang, H., et al., 2007. A surfactant-assisted hydrothermal deposition method for preparing highly dispersed W/γ-Al_2O_3 hydrodenitrogenation catalyst. J. Catal. 245 (2), 477–481. https://doi.org/10.1016/j.jcat.2006.11.003.

Fortain, D.P., Gauthier, T., Merdrignac, I., et al., 2010. Reactivity study of Athabasca vacuum residue in hydroconversion conditions. Catal. Today 150 (3–4), 255–263. https://doi.org/10.1016/j.cattod.2009.10.002.

Gafurov, M.R., Mukhambetov, I.N., Yavkin, B.V., et al., 2015. Quantitative analysis of lewis acid centers of γ-Alumina by using EPR of the adsorbed anthraquinone as a probe molecule: comparison with the pyridine, carbon monoxide IR, and TPD of ammonia. J. Phys. Chem. 119 (49), 27410–27415. https://doi.org/10.1021/acs.jpcc.5b09759.

Hensen, E.J.M., Kooyman, P.J., Meer, Y.V.D., et al., 2001. The relation between morphology and hydrotreating activity for supported MoS_2 particles. J. Catal. 199 (2), 224–235. https://doi.org/10.1006/jcat.2000.3158.

Jiang, Y.X., Wang, D.G., Li, J.H., et al., 2017. Designing MoS_2 nanocatalysts with increased exposure of active edge sites for anthracene hydrogenation reaction. Catal. Sci. Technol. 7 (14), 2998–3007. https://doi.org/10.1039/C7CY01026E.

Kang, K.H., Kim, G.T., Park, S., et al., 2019. A review on the Mo-precursors for catalytic hydroconversion of heavy oil. J. Ind. Eng. Chem. 76, 1–16. https://doi.org/10.1016/j.jiec.2019.03.022.

Kang, K.H., Nguyen, N.T., Seo, P.W., et al., 2020. Slurry-phase hydrocracking of heavy oil over Mo precursors: effect of triphenylphosphine ligands. J. Catal. 384, 106–121. https://doi.org/10.1016/j.jcat.2020.02.007.

Kasztelan, S., Toulhoat, H., Grimblot, J., et al., 1984. A geometrical model of the active phase of hydrotreating catalysts. Applied Catalysis A General 13 (1), 127–159. https://doi.org/10.1016/S0166-9834(00)83333-3.

Kim, S.H., Kim, K.D., Lee, Y.K., 2017. Effects of dispersed MoS_2 catalysts and reaction conditions on slurry phase hydrocracking of vacuum residue. J. Catal. 347, 127–137. https://doi.org/10.1016/j.jcat.2016.11.015.

Kim, S.H., Kim, K.D., Lee, D.H., et al., 2018. Structure and activity of dispersed Co, Ni, or Mo sulfides for slurry phase hydrocracking of vacuum residue. J. Catal. 364, 131–140. https://doi.org/10.1016/j.jcat.2018.05.002.

Leyva, C., Ancheyta, J., Mariey, L., et al., 2014. Characterization study of NiMo/SiO_2-Al_2O_3 spent hydroprocessing catalysts for heavy oils. Catal. Today 220–222, 89–96. https://doi.org/10.1016/j.cattod.2013.10.007.

Leyva, C., Rana, M.S., Trejo, F., et al., 2007. On the use of acid-base-supported catalysts for hydroprocessing of heavy petroleum. Ind. Eng. Chem. Res. 46 (23), 7448–7466. https://doi.org/10.1021/ie070128q.

Leyva, C., Rana, M.S., Trejo, F., et al., 2009. NiMo supported acidic catalysts for heavy oil hydroprocessing. Catal. Today 141 (1–2), 168–175. https://doi.org/10.1016/j.cattod.2008.03.030.

Liu, B., Zhao, K., Chai, Y., et al., 2019. Slurry phase hydrocracking of vacuum residue in the presence of presulfided oil-soluble MoS_2 catalyst. Fuel 246, 133–140. https://doi.org/10.1016/j.fuel.2019.02.114.

Liu, D., Kong, X., Li, M.Y., et al., 2009. Study on a water-soluble catalyst for slurry-phase hydrocracking of an atmospheric residue. Energy Fuel. 23 (2), 958–961. https://doi.org/10.1021/ef800653y.

Liu, S.J., Liang, X., Zhang, J., et al., 2017. Temperature sensitive synthesis of γ-Al_2O_3 support with different morphologies for CoMo/γ-Al_2O_3 catalysts for hydrodesulfurization of thiophene and 4,6-dimethyldibenzothiophene. Catal. Sci. Technol. 7 (2), 466–480. https://doi.org/10.1039/C6CY02241C.

Liu, X.M., Li, X., Yan, Z.F., 2012. Facile route to prepare bimodal mesoporous γ-Al_2O_3 as support for highly active CoMo-based hydrodesulfurization catalyst. Appl. Catal., B: Environmental 121– 122, 50–56. https://doi.org/10.1016/j.apcatb.2012.03.024.

Looi, P.Y., Mohamed, A.R., Tye, C.T., 2012. Hydrocracking of residual oil using molybdenum supported over mesoporous alumina as a catalyst. Chem. Eng. J. 181–182, 717–724. https://doi.org/10.1016/j.cej.2011.12.080.

Luo, H., Deng, W.N., Gao, J.J., et al., 2011. Dispersion of water-soluble catalyst and its influence on the slurry-phase hydrocracking of residue. Energy Fuel. 25 (3), 1161–1167. https://doi.org/10.1021/ef1014378.

Lv, Y.P., Wang, X.L., Gao, D.W., et al., 2018. Hierarchically porous ZSM-5/SBA-15 zeolite: tuning pore structure and acidity for enhanced hydro-upgrading of FCC gasoline. Ind. Eng. Chem. Res. 57 (42), 14031–14043. https://doi.org/10.1021/acs.iecr.8b02952.

Ma, Y.D., Wang, Y.R., Wu, W.Q., et al., 2021. Slurry-phase hydrocracking of a Decalin–Phenanthrene mixture by MoS_2/SiO_2–ZrO_2 bifunctional catalysts. Ind. Eng. Chem. Res. 60 (1), 230–242. https://doi.org/10.1021/acs.iecr.0c04999.

Manek, E., Haydary, J., 2017. Hydrocracking of vacuum residue with solid and dispersed phase catalyst: modeling of sediment formation and hydrodesulfurization. Fuel Process. Technol. 159, 320–327. https://doi.org/10.1016/j.fuproc.2017.02.003.

Morawski, I., Mosiewski, J.M., 2006. Effects of parameters in Ni–Mo catalysed hydrocracking of vacuum residue on composition and quality of obtained products. Fuel Process. Technol. 87 (7), 659–669. https://doi.org/10.1016/j.fuproc.2006.01.006.

Nguyen, T.S., Fayolle, M.T., Lacroix, M., et al., 2015. Promotion effects with dispersed catalysts for residue slurry hydroconversion. Fuel 160 (15), 50–56. https://doi.org/10.1016/j.fuel.2015.07.012.

Ninh, T., Massin, L., Laurenti, D., et al., 2011. A new approach in the evaluation of the support effect for NiMo hydrodesulfurization catalysts. Appl. Catal. Gen. 407 (1–2), 29–39. https://doi.org/10.1016/j.apcata.2011.08.019.

Omajali, J.B., Hart, A., Walker, M., et al., 2017. *In-situ* catalytic upgrading of heavy oil using dispersed bionanoparticles supported on gram-positive and gram-negative bacteria. Appl. Catal. B Environ. 203, 807–819. https://doi.org/10.1016/j.apcatb.2016.10.074.

Pham, H.H., Lim, S.H., Go, K.S., et al., 2022. Modeling and simulation of a bench-scale bubble column reactor for slurry phase hydrocracking of vacuum residue. Fuel 310, 122481–122493. https://doi.org/10.1016/j.fuel.2021.122481.

Phung, T.K., Busca, G., 2015. Diethyl ether cracking and ethanol dehydration: acid catalysis and reaction paths. Chem. Eng. J. 272, 92–101. https://doi.org/10.1016/j.cej.2015.03.008.

Prajapati, R., Kohli, K., Maity, S.K., 2021. Slurry phase hydrocracking of heavy oil and residue to produce lighter fuels: an experimental review. Fuel 288, 119686–119709. https://doi.org/10.1016/j.fuel.2020.119686.

Prajapati, R., Kohli, K., Maity, S.K., 2022. Role of catalyst defect sites towards product

selectivity in the upgrading of vacuum residue. Fuel 314, 123062–123072. https://doi.org/10.1016/j.fuel.2021.123062.
Purón, H., Pinilla, J.L., Berrueco, C., et al., 2013. Hydrocracking of Maya vacuum residue with NiMo catalysts supported on mesoporous alumina and silica–alumina. Energy Fuel. 27 (7), 3952–3960. https://doi.org/10.1021/ef400623f.
Saab, R., Polychronopoulou, K., Zheng, L., et al., 2020. Synthesis and performance evaluation of hydrocracking catalysts: a review. J. Ind. Eng. Chem. 89 (25), 83–103. https://doi.org/10.1016/j.jiec.2020.06.022.
Sánchez, J., Moreno, A., Mondragón, F., et al., 2018. Morphological and structural properties of MoS_2 and MoS_2-amorphous silica-alumina dispersed catalysts for slurry-phase hydroconversion. Energy Fuel. 32 (6), 7066–7077. https://doi.org/10.1021/acs.energyfuels.8b01081.
Schweitzer, J.M., Rey, J., Bignaud, C., et al., 2022. Multiscale modeling as a tool for the prediction of catalytic performances: the case of *n*-heptane hydroconversion in a large-pore zeolite. ACS Catal. 12 (2), 1068–1081. https://doi.org/10.1021/acscatal.1c04707.
Tang, B., Li, S., Song, W.C., et al., 2019. Hierarchical FAU-type hafnosilicate zeolite as a robust lewis acid catalyst for catalytic transfer hydrogenation. ACS Sustain. Chem. Eng. 7 (19), 16329–16343. https://doi.org/10.1021/acssuschemeng.9b03347.
Tsubaki, N., Chang, J., Yoneyama, Y., et al., 2002. Catalyst development for hydrothermal cracking of heavy oil effects of support and potassium salt additive. J. Jpn. Petrol. Inst. 45 (2), 77–83. https://doi.org/10.1627/jpi.45.77.
Valla, M., Rossini, A.J., Caillot, M., et al., 2015. Atomic description of the interface between silica and alumina in aluminosilicates through dynamic nuclear polarization surface-enhanced NMR spectroscopy and first-principles calculations. J. Am. Chem. Soc. 137 (33), 10710–10719. https://doi.org/10.1021/jacs.5b06134.
Wang, A.J., Wang, Y., Kabe, T., et al., 2002. Hydrodesulfurization of dibenzothiophene over siliceous MCM-41-supported catalysts: II. Sulfided Ni–Mo catalysts. J. Catal. 210 (2), 319–327. https://doi.org/10.1006/jcat.2002.3674.
Weitkamp, J., 2012. Catalytic hydrocracking mechanisms and versatility of the process. ChemCatChem 4 (3), 292–306. https://doi.org/10.1002/cctc.201100315.
Yue, Y.Y., Niu, P.L., Jiang, L.L., et al., 2016. Acid-modified natural bauxite mineral as a cost-effective and high-efficient catalyst support for slurry-phase hydrocracking of high-temperature coal tar. Energy Fuel. 30 (11), 9203–9209. https://doi.org/10.1021/acs.energyfuels.6b01869.
Yue, Y.Y., Li, J.W., Dong, P., et al., 2018. From cheap natural bauxite to high-efficient slurry-phase hydrocracking catalyst for high temperature coal tar: a simple hydrothermal modification. Fuel Process. Technol. 175, 123–130. https://doi.org/10.1016/j.fuproc.2018.03.006.
Zhang, C., Liu, X.Y., Liu, T.F., et al., 2019. Optimizing both the $CoMo/Al_2O_3$ catalyst and the technology for selectivity enhancement in the hydrodesulfurization of FCC gasoline. Appl. Catal. Gen. 575, 187–197. https://doi.org/10.1016/j.apcata.2019.02.025.
Zheng, P., Xiao, C.K., Song, S.T., et al., 2021. DFT insights into the hydrodenitrogenation mechanism of quinoline catalyzed by different Ni-promoted MoS_2 edge sites: effect of the active phase morphology. J. Hazard Mater. 411, 125127–125138. https://doi.org/10.1016/j.jhazmat.2021.125127.
Zheng, X.H., Li, Y.L., Zhang, L.Y., et al., 2019. Insight into the effect of morphology on catalytic performance of porous CeO_2 nanocrystals for H_2S selective oxidation. Appl. Catal. B Environ. 252, 98–110. https://doi.org/10.1016/j.apcatb.2019.04.014.